Article

Nonreciprocity of Optical Absorption in the Magnetoelectric Antiferromagnet CuB$_2$O$_4$

Kirill N. Boldyrev [1], **Anastasiia D. Molchanova** [1], **Alexey R. Nurmukhametov** [2], **Mikhail V. Eremin** [2], **Roman V. Pisarev** [3] **and Marina N. Popova** [1,*]

1 Institute of Spectroscopy, Russian Academy of Sciences, Troitsk, Moscow 108840, Russia;
kn.boldyrev@gmail.com (K.N.B.); nastyamolchanova@list.ru (A.D.M.)
2 Institute of Physics, Kazan Federal University, Kazan 420008, Russia; srgalex@list.ru (A.R.N.);
eremikhail@yandex.com (M.V.E.)
3 Ioffe Physical-Technical Institute RAS, St. Petersburg 194021, Russia
* Correspondence: popova@isan.troitsk.ru

Abstract: The change in the absorption spectra due to reversal of the direction of light propagation (nonreciprocity of absorption) is a consequence of a simultaneous violation of both time-reversal and spatial-inversion symmetries. Here, we report on a high-resolution spectroscopic study of absorption nonreciprocity in the noncentrosymmetric multiferroic CuB$_2$O$_4$ below the antiferromagnetic transition temperature T_N = 21 K in the commensurate phase in magnetic fields up to 0.5 T. The study was performed in a broad spectral region covering several exciton transitions, which all are followed by an anomalously rich structure due to the multiple exciton-magnon-phonon satellites. Two components were resolved for the spectral line near 1.4 eV corresponding to the exciton transition between the ground and the first excited state. A quantitative theory of the optical absorption and nonreciprocity at this line was developed. The theory takes into account the interference between the electric and magnetic dipole contributions to the absorption and gives an adequate explanation of the relevant effects.

Keywords: copper metaborate CuB$_2$O$_4$; high-resolution optical spectroscopy; doublet structure of 1.4 eV line; nonreciprocal directional dichroism; quantitative theory

1. Introduction

The assumption that copper metaborate CuB$_2$O$_4$ belongs to the class of magneto-electrics (multiferroics) was put forward by the authors in [1]. This assumption, as well as the fact that the spatial magnetic symmetry group of the crystal admits the presence of magnetoelectric phenomena [2,3], prompted the authors of [4] to study the temperature dependences of dielectric permittivity at different orientations of the external magnetic field. The results of this study have shown that the linear magnetoelectric coupling in CuB$_2$O$_4$ is small or even absent. However, the static magnetoelectric effects were confidently observed in slightly Ni-doped Cu$_{1-x}$Ni$_x$B$_2$O$_4$ (x = 0.027) crystals. Specifically, the plots of electric polarization measurements for this compound were presented in [5], and possible mechanisms of static magnetoelectric coupling in Cu$_{1-x}$Ni$_x$B$_2$O$_4$ crystals were analyzed in [6]. Microscopic calculations showed that the magnetoelectric effects found in [5] for Cu$_{1-x}$Ni$_x$B$_2$O$_4$ were due to the features of the electronic structure of Ni^{2+}($3d^8$) ions rather than copper Cu^{2+}($3d^9$) ions [6]. The magnetoelectric coupling parameters of Cu^{2+} ions in CuB$_2$O$_4$ estimated in [6] were relatively small, which agrees with the experimental results presented in [4].

In contrast to static magnetoelectric effects, dynamic optical effects, such as antiferromagnetic linear dichroism, nonreciprocal directional dichroism (NDD), and one-way transparency, at frequencies in the region of the 1.405 eV exciton transition were clearly demonstrated in [7–10]. A doublet structure of the 1.405 eV absorption line of magnetically

ordered CuB_2O_4 was found in [9]. To explain the detected magnetoelectric phenomena in CuB_2O_4, both phenomenological (group-theoretical) and microscopic (quantum-mechanical) approaches were used in [11–13]. The gigantic directional asymmetry of luminescence discovered in [14] was recently discussed in [15]. Having calculated the probabilities of magnetic and electric dipole transitions, the authors constructed radiation asymmetry diagrams for different directions of the external magnetic field.

In the present work, the phenomenon of nonreciprocity on both components of the fine structure of the 1.405 eV exciton line in the absorption spectra of CuB_2O_4 is studied both experimentally and theoretically. In previous experimental studies of nonreciprocity on CuB_2O_4, the fine structure was not resolved, apparently due to insufficient spectral resolution of the used equipment. We also studied the NDD effect in the previously unconsidered case of an external magnetic field directed along the tetragonal axis *c* of the crystal. An additional novelty of our study is in the reconstruction of the real line shape distorted by too strong absorption near the line maximum. This allowed us to obtain reliable quantitative information about the NDD effect.

2. Crystal Structure, Magnetism, and Optical Properties of CuB_2O_4

The copper metaborate CuB_2O_4 crystallizes in noncentrosymmetric tetragonal structure characterized by the space group $I\bar{4}2d$, $Z = 12$ [16]. With 42 atoms in the unit cell, it has a very rich and complicated phonon spectrum, see [17]. A schematic picture of the unit cell presented in Figure 1 shows the 4*b* and 8*d* Cu^{2+} ions surrounded by the nearest oxygens. The magnetic Cu^{2+} ions (electronic shell $3d^9$) with $S = 1/2$, $L = 0$ occupy two nonequivalent 4*b* and 8*d* crystallographic sites with the S_4 and C_2 point group symmetry, respectively [16]. In both of these sites, the copper ions are at the centers of almost ideal planar squares that are isolated, i.e., do not have common oxygen ions. Whereas the 4*b* CuO_4 squares are in the *ab* plane, the 8*d* CuO_4 plane squares are parallel to the *ac* or *bc* planes.
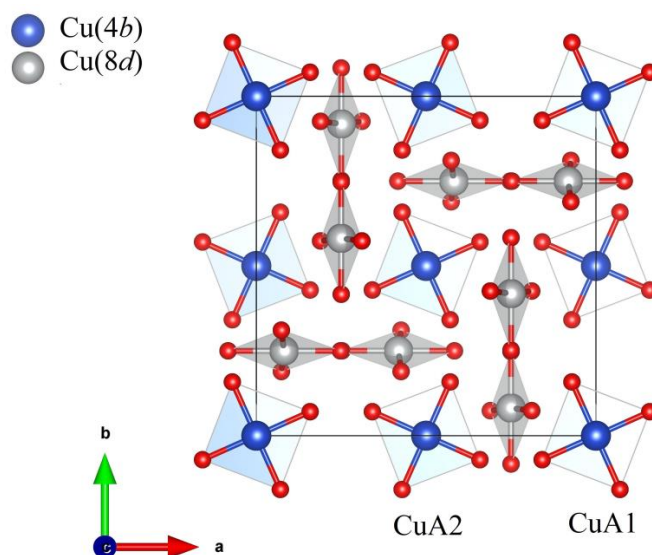

Figure 1. Projection of the CuO_4 units onto the *ab* plane of the tetragonal CuB_2O_4 structure. Boron atoms are not shown. For the 4*b* CuA1 (CuA2) positions, the local coordinate system is rotated counterclockwise by an angle $\varphi = 20.9°$ ($-20.9°$) around the tetragonal *c* axis, with respect to the crystallographic system. Thin black lines show the borders of the unit cell.

In fact, the 4*b* and 8*d* copper magnetic subsystems in CuB_2O_4 are almost independent from one another and, consequently, their magnetic and optical properties are substantially different. The "strong" magnetic Cu(4*b*) subsystem spontaneously orders at the Néel temperature $T_N = 21$ K into an easy *ab* plane antiferromagnetic commensurate structure. Two types of 90° antiferromagnetic domains are possible, with the antiferromagnetic vector parallel to either [110] or [$\bar{1}$10] directions. Due to the Dzyaloshinskii-Moriya interaction, there

is a weak ferromagnetic moment perpendicular to the antiferromagnetic spins [2,18–20]. The "weak" Cu(8d) magnetic subsystem is quasi-one-dimensional [2,21]. While the Cu(4b) magnetic moments reach the value $\mu_{Cu(b)}$ = 0.86 μ_B (μ_B is the Bohr magneton) at 12 K, the Cu(8d) ions at the same temperature have a small magnetic moment $\mu_{Cu(d)}$ = 0.20 μ_B along the z axis. It starts to grow only below the temperature T^*~10 K of the phase transition from the commensurate into an incommensurate helical phase, mounting to the value $\mu_{Cu(d)}$ = 0.54 μ_B at 2 K [2]. The Cu(8d) magnetic moments are not completely ordered and fluctuate even at the lowest temperatures [2]. A splitting of the phase transition at T^* into two successive transitions (T_1^* = 8.5 K and T_2^* = 7.9 K) and a possible existence of elliptical helical spin structures were revealed by measurements of optical linear dichroism in the isotropic crystallographic ab plane with the $\bar{4}$ symmetry [9]. Additional phase transitions were detected below 2 K [22,23]. The H–T phase diagram of CuB_2O_4 is very rich and complicated [23–25].

The optical properties of CuB_2O_4 are unusual and unique in several aspects. It is the only copper Cu^{2+} compound exhibiting very narrow well-resolved zero-phonon (ZP) lines for all d–d optical transitions [3,9,26]. An example of the absorption spectrum is presented in Figure 2a. Assignment of ZP lines related to the Cu(4b) and Cu(8d) subsystems was made by comparison with the second harmonic generation (SHG) spectra [3]. Thus, using optical techniques, one can selectively address a given transition of either 4b or 8d site. Each of the ZP lines is followed by an exceptionally rich vibronic structure [3,9,26] (see Figure 2a). As we show below, a magnon satellite is observed. Such well resolved and properly identified spectral structure delivers unique possibilities to study selectively NDD related to different types of d-d excitations.
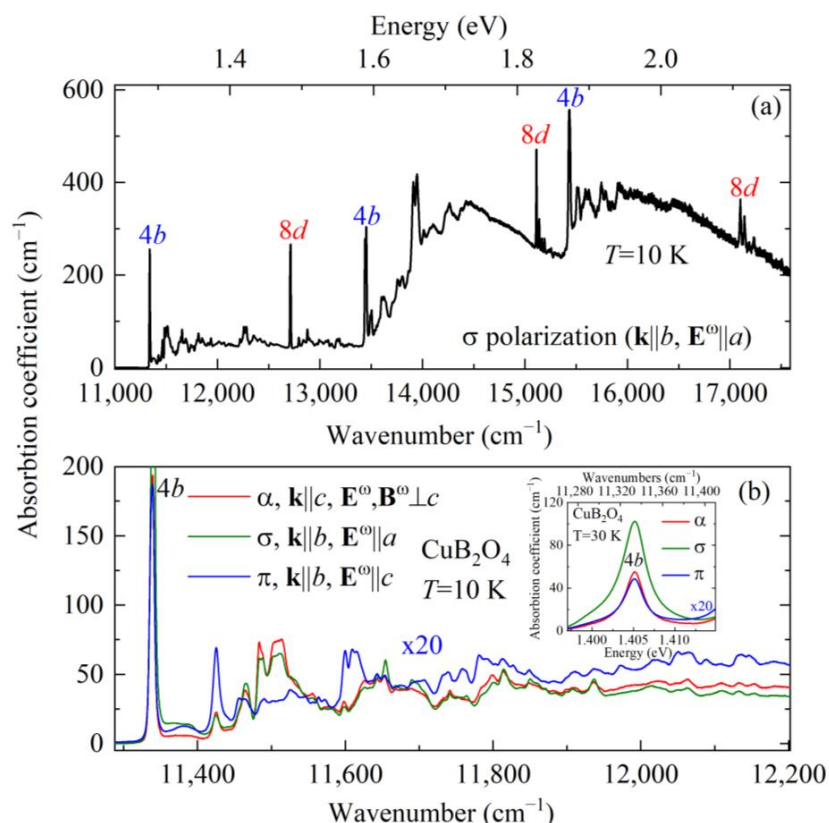
Figure 2. Absorption spectra of a CuB_2O_4 sample at the temperature 10 K in the spectral range (**a**) of all ZP lines in the σ (**k**||b, **E**$^\omega$||a) polarization; (**b**) of the lowest-frequency ZP line and accompanying vibronic satellites in the α (**k**||c, **E**$^\omega$,**B**$^\omega$⊥c, red curve), σ (**k**||b, **E**$^\omega$||a, green curve), and π (**k**||b, **E**$^\omega$||c, blue curve) polarizations. Inset shows the lowest-frequency ZP line in the polarized spectra of paramagnetic CuB_2O_4 at 30 K in the paramagnetic region.

3. Materials and Methods

Plane-parallel polished samples of (001) and (010) orientation with the thickness between 50 and 100 μm were prepared from CuB_2O_4 single crystals of good optical quality grown by a modified Kiropolus method [27]. Optical transmission spectra were measured with a resolution 0.8 cm^{-1} using a Bruker IFS 125HR Fourier spectrometer and a closed-cycle Cryomech ST403 cryostat. The temperature range was between 3.5 and 300 K and the spectra were studied in the α ($\mathbf{k} \| c$, $\mathbf{E}^\omega$, $\mathbf{B}^\omega \perp c$), σ ($\mathbf{k} \| b$, $\mathbf{E}^\omega \| a$), and π ($\mathbf{k} \| b$, $\mathbf{E}^\omega \| c$) polarizations. The (010)-oriented sample was studied also in an external magnetic field $\pm\mathbf{B}$ (0 < B < 0.5 T) in the Faraday ($\mathbf{k} \| \mathbf{B} \| b$) and Voigt ($\mathbf{k} \| b$, $\mathbf{B} \| c$ or $\mathbf{B} \| a$) geometries. The value of NDD was defined as a ratio $[k(+\mathbf{B}) - k(-\mathbf{B})] / [k(+\mathbf{B}) + k(-\mathbf{B})]$, where $k(\pm\mathbf{B})$ is the absorption coefficient of light in the CuB_2O_4 crystal subjected to an external magnetic field $\mathbf{B}$.

4. Experimental Results

4.1. Polarized Absorption Spectra of CuB$_2$O$_4$ in Zero External Field

Figure 2a shows an overview spectrum of the electronic transitions between crystal-field-split $3d$ levels within two different $4b$ and $8d$ copper subsystems. The entire set of six ZP lines accompanied by vibronic satellites occupies the range between 11,000 and 19,000 cm^{-1} (1.4–2.4 eV). Figure 2b presents high-resolution absorption spectra in the α, σ, and π polarizations in the region of the lowest-frequency $4b$ ZP line at 11,340 cm^{-1} (1.405 eV), which was reported to show one-way transparency in the Voigt geometry $\mathbf{k} \| [\overline{1}00]$, $\mathbf{B} \| [110]$ at 4.2 K in the magnetic field of 53 T [10]. This line corresponds to the optical transition between the ground $|x^2 - y^2\rangle$ and the first excited $|xy\rangle$ orbital singlet states of Cu^{2+} ions in the $4b$ positions with the S_4 symmetry (see the scheme in Figure 3). Both these states transform according to the Γ_2 irreducible representation of the S_4 point symmetry group, and only magnetic dipole (MD) transitions for $\mathbf{B}^\omega \| c$ (in the σ polarization) are allowed. The spin-orbit coupling results in Kramers doublets of the same symmetry in the ground and excited states and relaxes the selection rules. In addition to the σ-polarized MD transition, the spin-orbit interaction allows α- and π-polarized MD transitions and also α- and σ-polarized electric dipole (ED) transitions, as is illustrated in Figure 3. Thus, the integral intensity of the considered $4b$ spectral line in different polarizations, I_j (j = α, σ, π), is proportional to the following squared modules of matrix elements:

$$
\begin{aligned}
I_\alpha &\sim |<d_a E^\omega_a + d_b E^\omega_b + m_a B^\omega_a + m_b B^\omega_b>|^2 \\
I_\sigma &\sim |<d_a E^\omega_a + d_b E^\omega_b + m_c B^\omega_c>|^2 \\
I_\pi &\sim |<m_a B^\omega_a + m_b B^\omega_b + d_c E^\omega_c>|^2,
\end{aligned}
\tag{1}
$$

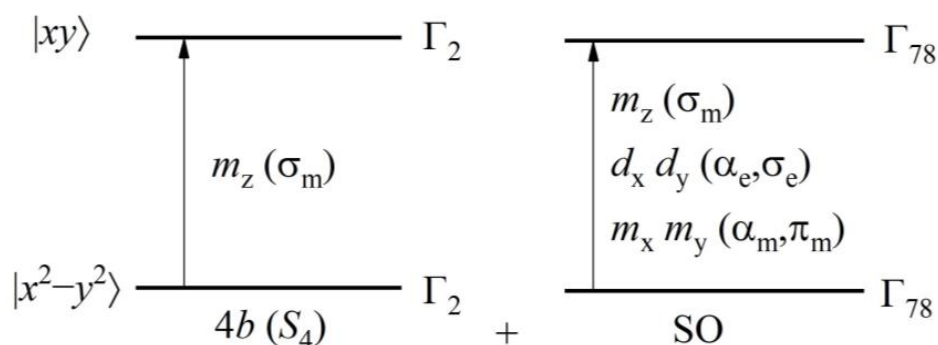where d_i and m_i (i = a, b, c) are components of the ED and MD moments, respectively.

Figure 3. Schematic diagram of Cu^{2+}-ion levels and optical transitions responsible for the lowest-frequency $4b$ exciton line.

Experimental values in the paramagnetic region of CuB_2O_4 are given in Table 1. By comparing these values with Equation (1), we conclude that for the lowest-frequency exciton transition at 1.405 eV,

$$d_c \ll d_a, d_b, \quad m_a, m_b \ll d_a, d_b, \quad m_c > d_a, d_b. \tag{2}$$

Table 1. Experimental values of integral absorption intensities $I_j = \int k(\nu)d\nu$, $j = \alpha, \sigma, \pi$ (in cm^{-2}) of the exciton spectral line at 1.405 eV for paramagnetic CuB_2O_4 at $T = 25$ K in zero external magnetic field, at the α, σ, and π polarizations.

	I_α $(\mathbf{k}\|c)$	I_σ $(\mathbf{k}\|b, \mathbf{E}^\omega\|a)$	I_π $(\mathbf{k}\|b, \mathbf{E}^\omega\|c)$
1st 4b line (1.405 eV)	1497	4830	84

A rich polarization-dependent vibronic structure is observed at the high-frequency side of the ZP line at 11,340 cm^{-1} (see Figure 2b). Most of the sharp peaks in the spectra can be attributed to electronic transitions with simultaneous creation of lattice phonons at the Γ point [17]. The whole structure almost does not change in the temperature interval between 35 and 3.5 K, with the exception of the lowest-frequency satellite of the 11,340 cm^{-1} ZP line occupying the range between ~11,350 and 11,400 cm^{-1} at low temperatures. Figure 4a,b display a behavior of the spectrum in this range with lowering the temperature. Drastic changes occur at this high-frequency wing of the ZP line. Below T_N, a well-defined shoulder is formed but, below the temperature $T^* \approx 10$ K corresponding to a transition into the incommensurate helical phase, formation of a gap between the ZP line and the discussed satellite is clearly observed, in line with appearance of a gap $\Delta E \approx 2.7$ meV (21.8 cm^{-1}) below T^* in the spectrum of spin excitations of CuB_2O_4 [28]. The total width of the satellite, 8 meV (64 cm^{-1}) coincides with the total width of the magnon branch, which further supports our interpretation. A single photon produces a pair of exciton and magnon with the wave vectors $\mathbf{k}$ and $-\mathbf{k}$, respectively. As the excitons corresponding to the d–d transitions of isolated Cu^{2+} ions are almost dispersionless, the total spectral width of the discussed satellite is due to the total width of the magnon branch. Thus, we can reasonably interpret the high-frequency satellite of the 11,340 cm^{-1} ZP line as a magnon sideband.

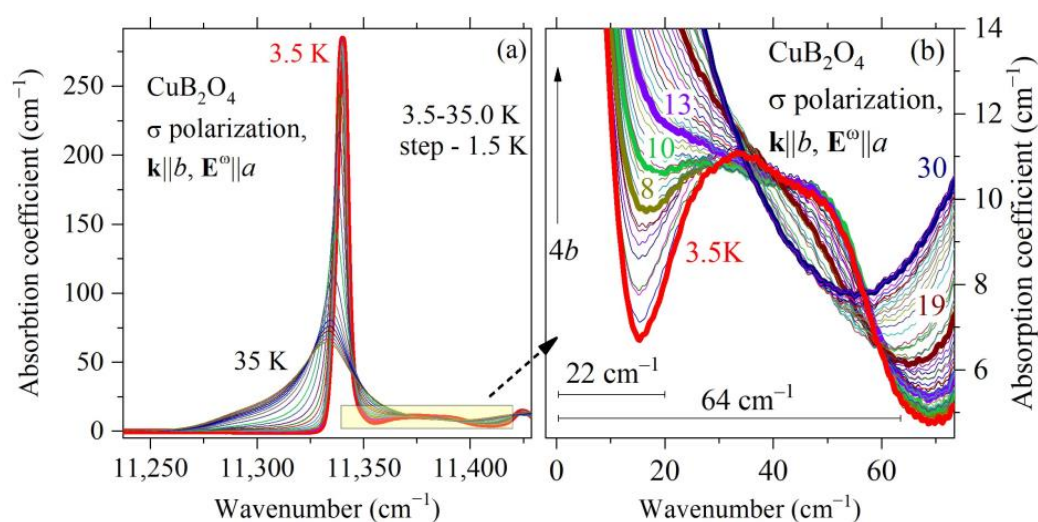**Figure 4.** Temperature dependence of (**a**) the lowest-frequency ZP exciton line and (**b**) its nearest higher-frequency broad magnon satellite.

4.2. Absorption Nonreciprocity in an External Magnetic Field

Further, we show and discuss our results on the NDD effect (nonreciprocity) in the case of an external magnetic field **B** applied along the c or b axes of the CuB_2O_4 crystal.

Figure 5a,b shows the absorption spectra in the Voigt geometry, σ polarization ($\mathbf{B}\|c$, $\mathbf{k}\|b$, $\mathbf{E}^{\omega}\|a$), $B = \pm 0.2$ T. The difference in the spectra is clearly observed, the largest (of about 900 cm^{-1}) being at the first 4b exciton line. The spectrum of NDD (nonreciprocity) is presented in Figure 5c,d. Similar absorption and NDD spectra are observed for the Faraday geometry, σ polarization ($\mathbf{k}\|\mathbf{B}\|b$, $\mathbf{E}^{\omega}\|a$), $B = \pm 0.2$ T. NDD of different values and signs is observed at all 4b and 8d exciton transitions and, as is important, also at the phonon and magnon satellites. At the vibronic transitions it has the same sign as at the exciton one but at the exciton-magnon transition the sign of NDD is reversed. It is also important to add that sharp peaks are superimposed on a broad NDD background which changes sign at about 13,800 cm^{-1}. As phonons are invariant to the time-reversal symmetry, the observation of NDD at vibronic transitions implies an existence of exciton-phonon bound states. The sign reversal for NDD at the exciton-magnon transition can be understood if we consider that the excitons and magnons participating in this transition have opposite wave vectors $\mathbf{k}$ and are coupled antiferromagnetically.
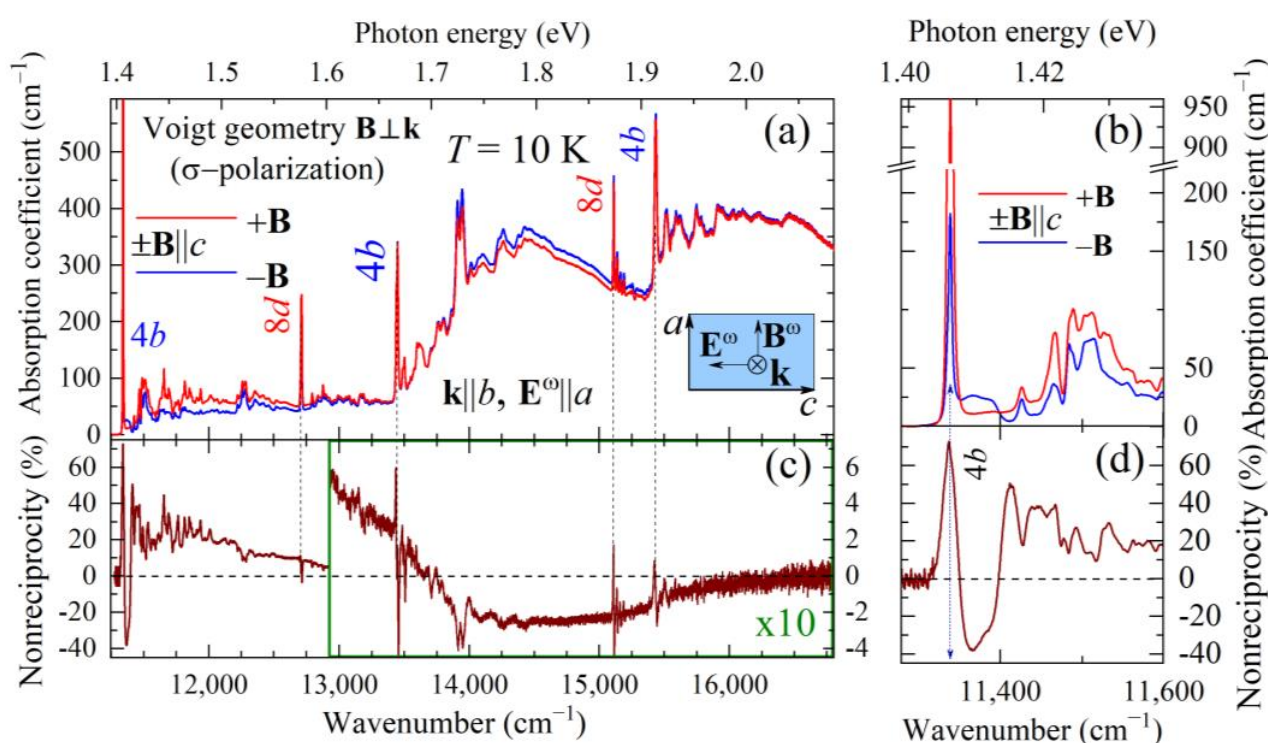

Figure 5. (**a**,**b**) Absorption and (**c**,**d**) NDD spectra of CuB$_2$O$_4$ at T = 10 K ($T^* < T < T_{\mathrm{N}}$) in an external magnetic field directed along the c axis of the crystal, $\mathbf{B}\|c$, $B = \pm 0.2$ T, the Voigt geometry $\mathbf{k}\|b$, σ polarization $\mathbf{E}^{\omega}\|a$. (**a**,**c**) The whole spectral range of the 4b and 8d exciton transitions and (**b**,**d**) region near the lowest-frequency 4b exciton transition at an expanded scale.

In the following, we focus our attention on the lowest-frequency 4b exciton ZP line near 1.405 eV exhibiting the largest NDD. In a general case, below T_{N} this line consists of two components centered at 11,336 and 11,341 cm^{-1} [9], and the line contour is well reproduced by a sum of two Voigt profiles (see Figure 6a). Absorption at the line 1.405 eV is strong in the σ polarization, so that $kl \approx 3.0$ at the line maximum for the thinnest sample we had ($l = 53$ μm), in zero external field $B = 0$. This implies the intensity of the transmitted light $I = I_0 e^{-kl} \approx 0.05 I_0$, which is at the noise level. When an external magnetic field is applied, in selected geometries of the experiment absorption diminishes for one direction of the field but further grows for the opposite direction, so that the line shape becomes distorted (see Figure 6b), and the absorption coefficient at the line maximum cannot be determined correctly. For weak and moderate absorption lines we applied the procedure of the line-shape modeling by the sum of two Voigt profiles. We used the same Voigt profiles

to reconstruct the true shape of strong lines, choosing such maximum intensities that the fit coincided with the measured contour at the line wings (up to $kl \approx 2.5$, see Figure 6b). Figure 6c presents the field dependence of kl at the maximum of the component 11,341 cm^{-1} in the $\mathbf{B}\|c$, $\mathbf{k}\|b$, $\mathbf{E}^{\omega}\|a$ Voigt geometry. It is perfectly linear down to $B = -0.182$ T in the region of negative fields where the line intensity diminishes with growth of the field intensity. At larger field values the line intensity remains unchanged. In the region of positive fields, the line intensity quickly saturates at the level $kl \approx 3.5$ showing a distorted profile. The described procedure for restoring the true line shape gives a linear dependence $kl(B)$ also for $B > 0$, until the saturation level is reached at $kl = 5.0$, as seen in Figure 6c. The corresponding value $k = 953$ cm^{-1} is given in Table 2. Note, however, that for too strong lines the procedure may not work. It is natural to assume that the line behavior at $B > 0$ is symmetric with that at $B < 0$, and the intensity reaches its maximal value at $B = +0.182$ T. The values of the absorption coefficient at the line maximum determined in this way are given in parentheses. Table 2 presents the results for different experimental geometries.
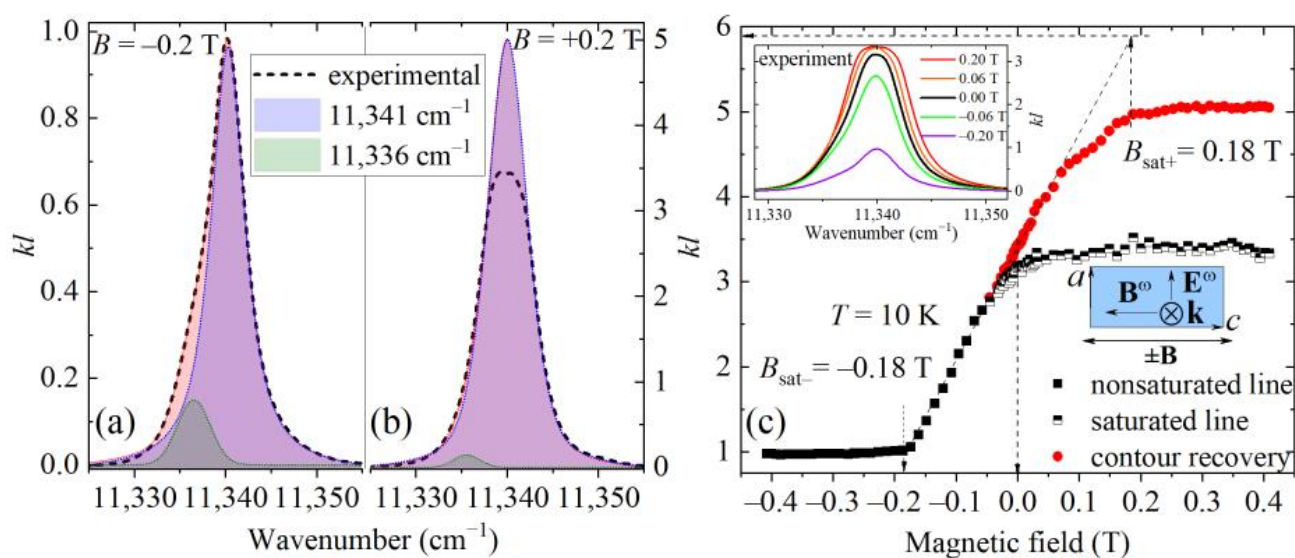
Figure 6. (**a**) Modeling of the line shape by a sum of two Voigt profiles and (**b**) reconstruction of the true shape of a strong line ($kl > 3.0$, see the text). (**c**) The field dependence of the absorbance kl at the maximum of the component 11,341 cm^{-1} in the $\mathbf{B}\|c$, $\mathbf{k}\|b$, $\mathbf{E}^{\omega}\|a$ Voigt geometry. In the area of positive magnetic field values, the data with (red symbols) and without (black and white symbols) the contour-reconstruction procedure is presented. Inset shows the experimental profiles for different field values.

Among the studied experimental geometries, NDD is reliably observed in two cases, namely, in the Voigt geometry $\mathbf{B}\|c$, $\mathbf{k}\|b$ and in the Faraday geometry $\mathbf{k}\|\mathbf{B}\|b$, with $\mathbf{E}^{\omega}\|a$ (σ polarization in both cases). This observation is in qualitative agreement with the results of previous studies [7,8], although the quantitative data differ.

Table 2. Experimental (cm^{-1}) and theoretical (squares of matrix element moduli in relative units) values of the absorption coefficients at the maxima of two components of the lowest-frequency $4b$ exciton line in the spectra of CuB$_2$O$_4$ at T = 10 K in an external magnetic field $|\mathbf{B}|$ = 0.2 T. The relative units are chosen so that in the Faraday geometry for the 11,341 cm^{-1} component at $\mathbf{B} \uparrow\uparrow [010]$, $\mathbf{L} = \mathbf{S}_{A1} - \mathbf{S}_{A2} \parallel [100]$, $\mathbf{E}^\omega \uparrow\uparrow [100]$, $\mathbf{B}^\omega \uparrow\uparrow [00\bar{1}]$ the calculated value is numerically equal to the experimental value.

Geometry of the Experiment		$|e_1\rangle$, 11,336 cm^{-1}		$|e_2\rangle$, 11,341 cm^{-1}	
		Exp.	Theor.	Exp.	Theor.
Voigt σ, $\mathbf{L} \parallel [110]$ $\mathbf{E}^\omega \uparrow\uparrow [100]$, $\mathbf{B}^\omega \uparrow\uparrow [00\bar{1}]$ $\mathbf{k} \parallel [010]$	$\mathbf{B} \uparrow\uparrow [001]$	-	76	-	222
	$\mathbf{B} \uparrow\uparrow [00\bar{1}]$	-	76	-	1040
Voigt σ, $\mathbf{L} \parallel [1\bar{1}0]$ $\mathbf{E}^\omega \uparrow\uparrow [100]$, $\mathbf{B}^\omega \uparrow\uparrow [00\bar{1}]$ $\mathbf{k} \parallel [010]$	$\mathbf{B} \uparrow\uparrow [001]$	25	76	953 (1094)	1040
	$\mathbf{B} \uparrow\uparrow [00\bar{1}]$	26	76	189	222
Voigt π, $\mathbf{L} \parallel [110]$ $\mathbf{E}^\omega \uparrow\uparrow [001]$, $\mathbf{B}^\omega \uparrow\uparrow [100]$ $\mathbf{k} \parallel [010]$	$\mathbf{B} \uparrow\uparrow [001]$	8	4	8	4
	$\mathbf{B} \uparrow\uparrow [00\bar{1}]$	5	4	11	4
Voigt σ, $\mathbf{L} \parallel [010]$ $\mathbf{E}^\omega \uparrow\uparrow [100]$, $\mathbf{B}^\omega \uparrow\uparrow [00\bar{1}]$ $\mathbf{k} \parallel [010]$	$\mathbf{B} \uparrow\uparrow [100]$	166	151	542	556
	$\mathbf{B} \uparrow\uparrow [\bar{1}00]$	154	151	554	556
Voigt π, $\mathbf{L} \parallel [010]$ $\mathbf{E}^\omega \uparrow\uparrow [001]$, $\mathbf{B}^\omega \uparrow\uparrow [100]$ $\mathbf{k} \parallel [010]$	$\mathbf{B} \uparrow\uparrow [100]$	15	0	0	7
	$\mathbf{B} \uparrow\uparrow [\bar{1}00]$	14	0	1	7
Faraday σ, $\mathbf{L} \parallel [100]$ $\mathbf{E}^\omega \uparrow\uparrow [100]$, $\mathbf{B}^\omega \uparrow\uparrow [00\bar{1}]$ $\mathbf{k} \parallel [010]$	$\mathbf{B} \uparrow\uparrow [010]$	0	1	127	127
	$\mathbf{B} \uparrow\uparrow [0\bar{1}0]$	0	0	1071 (1141)	1286
Faraday π, $\mathbf{L} \parallel [100]$ $\mathbf{E}^\omega \uparrow\uparrow [001]$, $\mathbf{B}^\omega \uparrow\uparrow [100]$ $\mathbf{k} \parallel [010]$	$\mathbf{B} \uparrow\uparrow [010]$	7	7	9	0
	$\mathbf{B} \uparrow\uparrow [0\bar{1}0]$	7	7	9	0

5. Discussion of Results and Theoretical Analysis of Nonreciprocity within the Scenario of Interference of Magnetic and Electric Dipole Transitions

For a theoretical analysis of the obtained experimental results, the energy levels, wave functions, and probabilities of electric and magnetic dipole transitions were calculated. In the unit cell there are four $4b$ positions of antiferromagnetically coupled copper CuA1 and CuA2 ions, which are pairwise equivalent [16]. Energy levels and wave functions for both positions were calculated by diagonalizing the Hamiltonian

$$\hat{\mathcal{H}} = \sum B_q^{(k)} C_q^{(k)} + \lambda(\hat{l}\hat{s}) + J_{gg}|g\rangle \langle g| \sum_{i=1}^{4} \langle \mathbf{s}_{Cu}\rangle \hat{s} + J_{ge}|e\rangle \langle e| \sum_{i=1}^{4} \langle \mathbf{s}'_{Cu}\rangle \hat{s} + \mu_B B(\hat{l} + 2\hat{s}). \quad (3)$$

Here, the parameter of the exchange interaction between the ground states of copper ions is assumed to be J_{gg} = 29 cm^{-1} [14], and the spin-orbit coupling parameter is $\lambda = -815$ cm^{-1} [29]; $\mathbf{B}$ is an external magnetic field. In addition to the energy operator from [15], Equation (3) also includes a term that takes into account the exchange interaction between copper ions in the first excited orbital state $|e\rangle$ and their nearest neighbors in the ground orbital state $|g\rangle$, which has recently been determined in [30] and is equal to $J_{ge} = -2.4$ cm^{-1}.

The calculations were carried out in local coordinate (LC) systems using a basis of all possible orbital $|\varepsilon\rangle \equiv |x^2 - y^2\rangle$, $|\zeta\rangle \equiv |xy\rangle$, $|\theta\rangle \equiv |3z^2 - r^2\rangle$, $|\eta\rangle \equiv |xz\rangle$, $|\xi\rangle \equiv |yz\rangle$ and spin $|\pm 1/2\rangle$ states. The LC system permits to choose the x and y axes so that $ImB_4^4 = 0$ and thus to reduce the number of parameters. LC system for CuA1 (CuA2) is rotated with respect to the crystallographic coordinate (CC) system by an angle $\varphi = 20.9°\ (-20.9°)$

around the *c* axis of the crystal (the angle is counted counterclockwise, see Figure 1). The crystal-field parameters in the CC system are related to the parameters in the LC system by the relations:

$$B'^{(k)}_q = B^{(k)}_q exp(-iq\varphi). \tag{4}$$

For both positions the crystal-field, parameters $B^{(k)}_q$ in the corresponding LC system are (in cm^{-1}) [6]:

$$B^{(2)}_0 = -17720, B^{(4)}_0 = 9940, B^{(4)}_4 = 14030. \tag{5}$$

The calculated wave functions of the ground and the first excited (1.4 eV) states are given in Appendix A.

It is assumed that the ED transitions in this compound arise due to the mixing of the Cu^{2+} states within the $3d^9$ ground configuration with the excited configuration $3d^84p$ and the configuration with charge transfer from the oxygen electronic orbitals to the copper $3d$ shell. The effective operator of the binding energy of $3d$ electrons with an electric field is written as follows:

$$\hat{H}_E = \sum_{\substack{k=2,4 \\ p=1,3,5 \\ t=\pm 2}} \left\{ E^{(1)} \hat{U}^{(k)} \right\}^{(p)}_t D^{(1k)p}_t \tag{6}$$

Here, the braces denote the direct product of the spherical components of the electric field $E^{(1)}_0 = E_z$; $E^{(1)}_{\pm 1} = \mp \left(E_x \pm i \cdot E_y \right) / \sqrt{2}$ and the unit tensor operator $U^{(k)}$. Due to the symmetry, only the following parameters $D^{(1k)p}_t$ are non-zero: $D^{(12)3}_{\pm 2}$, $D^{(14)3}_{\pm 2}$, and $D^{(14)5}_{\pm 2}$. $D^{(1k)p}_t$ were calculated for both positions in the CC system using the formulas given in [31,32]. The relationship between the parameters for CuA1 and CuA2 sites is explained in Appendix B. Relations between the parameters $D^{(1k)p}_t$ in the CC and LC systems are similar to (4):

$$D'^{(1k)p}_t = D^{(1k)p}_t exp(-it\varphi). \tag{7}$$

At the exciton transition under study, due to the peculiarity of the wave functions of the ground and excited states (see Appendix A), ED transitions appear due to the following four matrix elements:

$$\langle \varepsilon | \hat{H}_E | \eta \rangle = D_1 E_x - D_3 E_y, \tag{8}$$

$$\langle \varepsilon | \hat{H}_E | \xi \rangle = D_3 E_x + D_1 E_y,$$

$$\langle \zeta | \hat{H}_E | \eta \rangle = -D_2 E_x - D_4 E_y,$$

$$\langle \zeta | \hat{H}_E | \xi \rangle = D_4 E_x - D_2 E_y.$$

Here, the notations are the same as in [15], namely, D_i are the linear combinations of $D^{(1k)p}_t$. This allows one to reduce the number of model parameters to four quantities D_i. The matrix element values were estimated using the calculated values of $D^{(1k)p}_t$ and then refined to fit the experimental data of the present work and also the relative absorption line intensities given in Figure 2a of [10], described in [15]. In the LC system for the CuA1 position, the D_i values are (in Debye):

$$D_1 = 0.081, D_2 = 0.085, D_3 = 0.081, D_4 = 0.085. \tag{9}$$

The resulting set of parameters D_i does not allow unambiguous determination of all possible components of the effective dipole moment $D^{(1k)p}_t$, but is sufficient for calculating the absorption and luminescence spectra in the 1.4 eV region.

For calculating the magnetic dipole transitions, the standard operator was used:

$$\hat{H}_M = \mu_B \boldsymbol{B}^\omega (\hat{\boldsymbol{L}} + 2\hat{\boldsymbol{S}}), \tag{10}$$

also taking into account the relation between the magnetic field induction and the electric field strength in the light wave $\boldsymbol{B}^\omega = \sqrt{\varepsilon\mu}[\boldsymbol{k} \times \boldsymbol{E}^\omega]/k$, the refractive index is $\sqrt{\varepsilon\mu} = 1.75$ [26].

The calculated values of the matrix elements of the dipole moment components corresponding to the transitions between the ground $|g_1\rangle$ and the excited doublet states $|e_1\rangle$ and $|e_2\rangle$ in the CC system for $B = 0$ and $\boldsymbol{L} \parallel [110]$ are given in Table 3. They are in a qualitative agreement with the experimental relations (2) found from the analysis of polarized absorption spectra. The explicit form of the wave functions is presented in Appendix A. The wave functions $|e_1\rangle$ and $|e_2\rangle$ correspond to states with lower and higher energy, respectively. It is believed that the splitting is due to the action of the exchange (molecular) field from the surrounding magnetic ions in the ground states. According to Goodenough-Kanamori's rules, the exchange coupling of the excited state with the ground state of neighboring copper spins is considered to be ferromagnetic in nature.

Table 3. Matrix elements $\langle g_1|d_\alpha|e_{1,2}\rangle$ and $\langle g_1|m_\alpha|e_{1,2}\rangle$ of the operators of electric and magnetic dipole transitions in arbitrary units for CuA1 and CuA2.

	CuA1		CuA2	
	$\|e_1\rangle$, 11,336 cm^{-1}	$\|e_2\rangle$, 11,341 cm^{-1}	$\|e_1\rangle$, 11,336 cm^{-1}	$\|e_2\rangle$, 11,341 cm^{-1}
d_a	$-1230i$	-1102	$-1100i$	-1232
d_b	$-1100i$	1232	$-1230i$	1102
d_c	0	0	0	0
m_a	258	$258i$	-258	$-258i$
m_b	258	$-258i$	-258	$258i$
m_c	0	-3168	0	-3168

From Table 3, it is easy to understand the features of the interference of MD and ED transitions, as well as to understand in which polarizations of the light wave interference between MD and ED transitions does not occur. For example, it can be seen that in the polarizations B_a^ω, E_b^ω and B_b^ω, E_a^ω the manifestation of nonreciprocity is not expected, since the moduli of the matrix elements do not depend on the sign of terms, namely, $|m_a + d_b|^2 = |m_a - d_b|^2$. The results of calculating the total absorption intensity for electric and magnetic dipole transitions are shown in Table 2. Note that reversing the incident light vector $\boldsymbol{k}$ yields the same result as reversing the magnetic field $\boldsymbol{B}$ in the experiments. The former corresponds to the time inversion of the EM-interaction operator $\hat{H}_E + \hat{H}_M$, the latter can be thought of as the time inversion of the wave functions:

$$\langle\psi_1|H_E + H_M|\psi_2\rangle_{B\to-B} = (\langle\psi_1|T^+)(H_E + H_M)(T|\psi_2\rangle) = \langle\psi_1|(T^+(H_E + H_M)T)|\psi_2\rangle$$
$$= \langle\psi_1|(H_E + H_M)_{t\to-t}|\psi_2\rangle = \langle\psi_1|(H_E + H_M)_{k\to-k}|\psi_2\rangle = \langle\psi_1|H_E - H_M|\psi_2\rangle \tag{11}$$

As can be seen from Table 2, in most cases the results of the theoretical calculations correspond to the experimental results.

To conclude this Section, we note that in the Voigt geometry $\boldsymbol{B} \parallel [001]$, $\boldsymbol{k} \parallel [010]$, σ polarization ($\boldsymbol{E}^\omega \parallel [100]$) the calculated absorption coefficients for two types of domains $\boldsymbol{L} \parallel [110]$ and $\boldsymbol{L} \parallel [\bar{1}10]$ differ significantly at a given direction of the external magnetic field. The highest value of the absorption coefficient in $\boldsymbol{L} \parallel [110]$ ($\boldsymbol{L} \parallel [\bar{1}10]$) domains is achieved for $\boldsymbol{B} \upuparrows [00\bar{1}]$ ($\boldsymbol{B} \upuparrows [001]$) (see Table 2). An external magnetic field directed along the tetragonal axis c of the crystal does not disturb the 90° domain structure but allows its visualization using the interference effect of MD and ED transitions. With a given direction of the external magnetic field, one type of domain will be visible as dark regions while the other as bright ones. Technique of optical reading can be used to quickly read information from magnetic storage devices.

6. Conclusions

In our work, we presented and analyzed experimental results on absorption nonreciprocity of the magnetoelectric antiferromagnet CuB_2O_4. The study was performed within the spectroscopic range from 1.4 up to 2.4 eV where several exciton lines related to the $4b$ and $8d$ magnetic subsystems of the Cu^{2+} ions are observed. Experimental results were obtained using spectroscopic technique with higher spectral resolution than in previous studies, and this gave us the opportunity to significantly deepen the understanding of the optical absorption processes in CuB_2O_4. We concentrated our research on the lowest energy exciton absorption line at 1.405 eV that corresponds to the optical transition between the ground and the first excited state of the $4b$ Cu^{2+} subsystem. We show that this line below T_N is split into two spectrally-resolved components with the splitting value of ~0.6 meV (~5 cm^{-1}) even in zero external magnetic field. We developed a microscopic theoretical model of optical absorption and nonreciprocity of the 1.405 eV exciton line. The model shows that the splitting can be explained by the action of the exchange (molecular) field from the surrounding magnetic Cu^{2+} ions in their excited state. For the first time, we observed optical nonreciprocity on both components of this split exciton line, as well as in a Voigt geometry with an external magnetic field directed along the tetragonal axis c of the crystal. The model explains the observed effects by involving interference of MD and ED transitions which both contribute to absorption and nonreciprocity processes. The model also explains the experimental data on nonreciprocity observed earlier in [7,8,10] under conditions of a spectrally-unresolved structure of the same exciton absorption line. Important to note that nonreciprocity was also observed for higher in energy excitons and exciton-phonon satellites of the $4b$ subsystem, as well as for all $8d$ excitons and relevant satellites in partially disordered magnetic Cu^{2+} subsystem. We believe that our theoretical model for the energy interaction operator of a $3d$ electron with the electric field of the light wave can be applied for further analysis of nonreciprocity related to higher in energy transitions within the $4b$ antiferromagnetic Cu^{2+} subsystem in CuB_2O_4.

In conclusion, it is worth comparing dynamic magnetoelectric effects in the novel magnetoelectric compound CuB_2O_4 with the similar effects in the known perovskite-based multiferroics. Unlike CuB_2O_4, the optical absorption lines are broad there, so the study of dynamic magnetoelectric effects is performed mainly in the terahertz region of the spectrum. The nature of static and dynamic magnetoelectric coupling is discussed, as a rule, using the inverse Dzyaloshinskii–Moriya mechanism [33]. At the same time, experimental data have now been accumulated that require clarification and perhaps even revision of ideas about the mechanism of the observed dynamic effects in perovskite helimagnets [34]. In [35], as a result of studies of $DyMnO_3$ using terahertz time-domain spectroscopy, the authors have concluded that an improved understanding of the relationship between ED transitions and spins is needed. In this connection, it is logical to assume that the ideas we have developed about dynamic magnetoelectric coupling in CuB_2O_4 can be useful in modeling dynamic magnetoelectric effects both in perovskite helimagnets and in other magnetoelectrics containing ions with empty electron shells in positions without an inversion center.

Author Contributions: Conceptualization—M.V.E. and K.N.B.; formal analysis—A.D.M. and A.R.N.; funding acquisition—A.D.M., M.N.P. and M.V.E.; investigation—K.N.B., A.D.M., A.R.N. and M.V.E.; methodology—K.N.B. and M.V.E.; resources—R.V.P.; validation—K.N.B., A.D.M., M.N.P. and M.V.E.; visualization— K.N.B. and A.D.M.; writing—original draft—M.V.E. and M.N.P.; writing—review and editing—R.V.P., M.N.P. and A.R.N. All authors have read and agreed to the published version of the manuscript.

Institutional Review Board Statement: Not applicable.

Informed Consent Statement: Not applicable.

Data Availability Statement: The data that support the plots within the paper and other findings of this study are available from the corresponding author upon reasonable request.

Conflicts of Interest: The authors declare no conflict of interest.

Appendix A. Wave Functions of the Ground and the First Excited Doublets

The wave functions of the Zeeman doublet CuA1 (1.4 eV) calculated in the local coordinate system in an external field $B_c = 0.3$ T have the form:

$$
\begin{aligned}
|e_{1,2}\rangle &= 0.693 \cdot |xy, \pm\rangle \pm (0.64 \pm 0.286i) \cdot |xy, \mp\rangle \\
&\quad - (0.033 \mp 0.073i) \cdot |xz, \pm\rangle + 0.079i \cdot |xz, \mp\rangle \\
&\quad - (0.073 \pm 0.033i) \cdot |yz, \pm\rangle \pm 0.079 \cdot |yz, \mp\rangle \\
&\quad \pm 0.044i \cdot |x^2 - y^2, \pm\rangle \pm (0.018 \mp 0.040i) \cdot |x^2 - y^2, \mp\rangle
\end{aligned}
\tag{A1}
$$

The wave functions of the ground doublet are written as follows:

$$
\begin{aligned}
|g_{1,2}\rangle &= 0.702 \cdot |x^2 - y^2, \pm\rangle \mp (0.646 \pm 0.289i) \cdot |x^2 - y^2, \mp\rangle \\
&\quad \pm 0.048i \cdot |xy, \pm\rangle \mp (0.020 \mp 0.045i) \cdot |xy, \mp\rangle \\
&\quad + (0.016 \pm 0.007i) \cdot |xz, \pm\rangle \pm 0.017 \cdot |xz, \mp\rangle \\
&\quad - (0.007 \mp 0.016i) \cdot |yz, \pm\rangle - 0.017i \cdot |yz, \mp\rangle .
\end{aligned}
\tag{A2}
$$

When the action of exchange (molecular) fields is taken into account, the doublets split. The mean values of the spin operator for the respective states $|g_i\rangle$ and $|e_i\rangle$ are different due to the opposite direction of the exchange fields in the ground and excited states.

When the sign of the external field is switched, the direction of the spins in the domains is reversed. This was also noted in [14]. The reason for the change in the direction of the spins is associated with the presence of the Dzyaloshinskii-Moriya interaction, which leads to a slight canting of the neighboring copper spins. The magnetic field reverses the direction of the spins, "hooking" them to the vector of weak ferromagnetism. Thus, when the sign of the field changes (by -0.3 Tesla), the wave functions are reversed: $|g_{1,2}\rangle_{B_c<0} = |g_{2,1}\rangle_{B_c>0}$, $|e_{1,2}\rangle_{B_c<0} = |e_{2,1}\rangle_{B_c>0}$. ($B_c > 0$ and $B_c < 0$ correspond to the directions $[001]$ and $[00\bar{1}]$, respectively). As has already been noted in [10], the admixture of the orbital states $|xz\rangle$ and $|yz\rangle$ to the excited state due to the spin-orbit interaction is important. Due to this, ED transitions from the ground state are allowed. Note that in [10], Supplementary, the mixing of the ground state with the excited states was not taken into account at all. However, this is important for quantitative comparison of theory with experiment.

Appendix B. On the Difference between the Parameters of Electric Dipole Transitions for the Positions Cu(A1) and Cu(A2)

The parameters of ED transitions are calculated by the formula:

$$
D_t^{(1k)p} = \sum_j d^{(1k)p}(R_j) \cdot (-1)^t \cdot C_{-t}^{(p)}(\theta_j, \varphi_j)
\tag{A3}
$$

where $(-1)^t C_{-t}^{(p)}(\theta_j, \varphi_j) = \sqrt{4\pi/(2p+1)}\, Y_{p,t}^*(\theta_j, \varphi_j)$ are components of the spherical tensor that determines the position of the lattice ion in the position with number *j*.

According to the Neumann's principle, the symmetry operations that preserve the A1 copper ion must also preserve the parameters characterizing it, and the operations

that transfer the A1 ion to the A2 position must similarly transform the parameters. For example, the $\sigma_{[110]}$ operator transforms crystallographic coordinates as follows:

$$\sigma_{[110]}(a) = -b, \sigma_{[110]}(b) = -a, \sigma_{[110]}(c) = c. \tag{A4}$$

Parameters $D_t^{(1k)p}$ change as components of a spherical tensor $Y_{p,t}^*(\theta_j, \varphi_j)$. Consider, for example, $D_2^{(12)3}$:

$$\sigma_{[110]}\left(D_2^{(12)3}\right) \sim \sigma_{[110]}\left([a-ib]^3 c\right) = -\left[a^2-b^2\right]c + i\cdot 2abc = -D_2^{(12)3^*} \tag{A5}$$

Thus, $D_2^{(12)3}(A1) = -D_2^{(12)3^*}(A2)$. It is easy to see that operations 2_a, 2_b, and $\sigma_{[\bar{1}10]}$ yield the same result, while operation 2_c preserves $D_2^{(12)3}$. Similarly, one can obtain:

$$D_2^{(14)3}(A1) = -D_2^{(14)3^*}(A2) \text{ and } D_2^{(14)5}(A1) = -D_2^{(14)5^*}(A2).$$
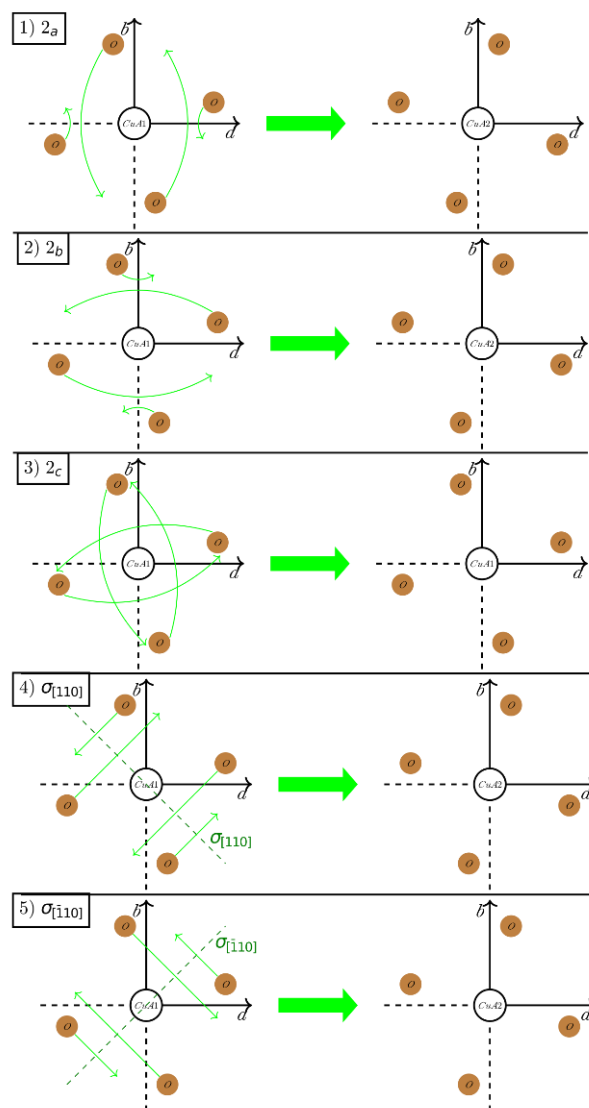

Figure A1. Explanations of the symmetry elements that transform the Cu(A1) position into the Cu(A2) position.

References

1. Fujita, T.; Fujimoto, Y.; Mitsudo, S.; Idehara, T.; Inoue, K.; Kishine, J.; Kousaka, Y.; Yano, S.; Akimitsu, J.; Motokawa, M. High Field ESR Measurements on the Chiral Spin System CuB_2O_4. *J. Phys. Conf. Ser.* **2006**, *51*, 111–114. [CrossRef]
2. Boehm, M.; Roessli, B.; Schefer, J.; Wills, A.S.; Ouladdiaf, B.; Lelièvre-Berna, E.; Staub, U.; Petrakovskii, G.A. Complex Magnetic Ground State of CuB_2O_4. *Phys. Rev. B* **2003**, *68*, 024405. [CrossRef]
3. Pisarev, R.; Sänger, I.; Petrakovskii, G.; Fiebig, M. Magnetic-Field Induced Second Harmonic Generation in CuB_2O_4. *Phys. Rev. Lett.* **2004**, *93*, 037204. [CrossRef] [PubMed]
4. Nénert, G.; Bezmaternykh, L.N.; Vasiliev, A.N.; Palstra, T.T.M. Magnetic, Structural, and Dielectric Properties of CuB_2O_4. *Phys. Rev. B* **2007**, *76*, 144401. [CrossRef]
5. Khanh, N.D.; Abe, N.; Kubo, K.; Akaki, M.; Tokunaga, M.; Sasaki, T.; Arima, T. Magnetic Control of Electric Polarization in the Noncentrosymmetric Compound $(Cu,Ni)B_2O_4$. *Phys. Rev. B* **2013**, *87*, 184416. [CrossRef]
6. Eremin, M.V.; Nurmukhametov, A.R. On the Magnetoelectric Coupling in $(Ni, Cu)B_2O_4$. *JETP Lett.* **2021**, *114*, 35–39. [CrossRef]
7. Saito, M.; Taniguchi, K.; Arima, T. Gigantic Optical Magnetoelectric Effect in CuB_2O_4. *J. Phys. Soc. Jpn.* **2008**, *77*, 013705. [CrossRef]
8. Saito, M.; Ishikawa, K.; Taniguchi, K.; Arima, T. Magnetic Control of Crystal Chirality and the Existence of a Large Magneto-Optical Dichroism Effect in CuB_2O_4. *Phys. Rev. Lett.* **2008**, *101*, 117402. [CrossRef]
9. Boldyrev, K.N.; Pisarev, R.V.; Bezmaternykh, L.N.; Popova, M.N. Antiferromagnetic Dichroism in a Complex Multisublattice Magnetoelectric CuB_2O_4. *Phys. Rev. Lett.* **2015**, *114*, 247210. [CrossRef]
10. Toyoda, S.; Abe, N.; Kimura, S.; Matsuda, Y.H.; Nomura, T.; Ikeda, A.; Takeyama, S.; Arima, T. One-Way Transparency of Light in Multiferroic CuB_2O_4. *Phys. Rev. Lett.* **2015**, *115*, 267207. [CrossRef]
11. Lovesey, S.W.; Staub, U. Calculated Chiral and Magneto-Electric Dichroic Signals for Copper Metaborate (CuB_2O_4) in an Applied Magnetic Field. *J. Phys. Condens. Matter* **2009**, *21*, 142201. [CrossRef] [PubMed]
12. Lovesey, S.W. Zeeman Spectrum, Magnetic Neutron Diffraction Pattern, and Dirac Multipoles for a Multiferroic Material CuB_2O_4. *Phys. Rev. B* **2016**, *94*, 094422. [CrossRef]
13. Nikitchenko, A.I.; Pisarev, R.V. Magnetic and Antiferromagnetic Nonreciprocity of Light Propagation in Magnetoelectric CuB_2O_4. *Phys. Rev. B* **2021**, *104*, 184108. [CrossRef]
14. Toyoda, S.; Abe, N.; Arima, T. Gigantic Directional Asymmetry of Luminescence in Multiferroic CuB_2O_4. *Phys. Rev. B* **2016**, *93*, 201109. [CrossRef]
15. Nurmukhametov, A.R.; Eremin, M.V. On the Theory of the Dynamic Magnetoelectric Coupling in CuB_2O_4. *J. Exp. Theor. Phys.* **2022**, *135*, 339–346. [CrossRef]
16. Martinez-Ripoll, M.; Martínez-Carrera, S.; García-Blanco, S. The Crystal Structure of Copper Metaborate, CuB_2O_4. *Acta Crystallogr. B* **1971**, *27*, 677–681. [CrossRef]
17. Pisarev, R.V.; Boldyrev, K.N.; Popova, M.N.; Smirnov, A.N.; Davydov, V.Y.; Bezmaternykh, L.N.; Smirnov, M.B.; Kazimirov, V.Y. Lattice Dynamics of Piezoelectric Copper Metaborate CuB_2O_4. *Phys. Rev. B* **2013**, *88*, 024301. [CrossRef]
18. Petrakovskii, G.; Velikanov, D.; Vorotinov, A.; Balaev, A.; Sablina, K.; Amato, A.; Roessli, B.; Schefer, J.; Staub, U. Weak Ferromagnetism in CuB_2O_4 Copper Metaborate. *J. Magn. Magn. Mater.* **1999**, *205*, 105–109. [CrossRef]
19. Boehm, M.; Roessli, B.; Schefer, J.; Ouladdiaf, B.; Amato, A.; Baines, C.; Staub, U.; Petrakovskii, G.A. A Neutron Scattering and MSR Investigation of the Magnetic Phase Transitions of CuB_2O_4. *Phys. B Condens. Matter* **2002**, *318*, 277–281. [CrossRef]
20. Roessli, B.; Schefer, J.; Petrakovskii, G.A.; Ouladdiaf, B.; Boehm, M.; Staub, U.; Vorotinov, A.; Bezmaternikh, L. Formation of a Magnetic Soliton Lattice in Copper Metaborate. *Phys. Rev. Lett.* **2001**, *86*, 1885–1888. [CrossRef]
21. Martynov, S.; Petrakovskii, G.; Roessli, B. Quasi-One-Dimensional Excitations of Copper Metaborate in the Commensurate Phase. *J. Magn. Magn. Mater.* **2004**, *269*, 106–112. [CrossRef]
22. Molchanova, A.D.; Boldyrev, K.N. High-Resolution Spectroscopy of Low-Temperature Phase Transitions in Copper Metaborate CuB_2O_4. *Opt. Spectrosc.* **2019**, *127*, 33–35. [CrossRef]
23. Pankrats, A.I.; Petrakovskii, G.A.; Popov, M.A.; Sablina, K.A.; Prozorova, L.A.; Sosin, S.S.; Szimczak, G.; Szimczak, R.; Baran, M. New Magnetic States in Copper Metaborate CuB_2O_4. *J. Exp. Theor. Phys. Lett.* **2003**, *78*, 569–573. [CrossRef]
24. Pankrats, A.; Petrakovskii, G.; Tugarinov, V.; Sablina, K.; Bezmaternykh, L.; Szymczak, R.; Baran, M.; Kundys, B.; Nabialek, A. Magnetic Phase Diagram of Copper Metaborate in Magnetic Field Parallel to C-Axis. *J. Magn. Magn. Mater.* **2006**, *300*, e388–e391. [CrossRef]
25. Petrova, A.E.; Pankrats, A.I. Copper Metaborate CuB_2O_4 Phase Diagrams Based on the Results of Measuring the Magnetic Moment. *J. Exp. Theor. Phys.* **2018**, *126*, 506–513. [CrossRef]
26. Pisarev, R.V.; Kalashnikova, A.M.; Schöps, O.; Bezmaternykh, L.N. Electronic Transitions and Genuine Crystal-Field Parameters in Copper Metaborate CuB_2O_4. *Phys. Rev. B* **2011**, *84*, 075160. [CrossRef]
27. Aleksandrov, K.S.; Sorokin, B.P.; Glushkov, D.A.; Bezmaternykh, L.N.; Burkov, S.I.; Belushchenko, S.V. Electromechanical Properties and Anisotropy of Acoustic Wave Propagation in CuB_2O_4 Copper Metaborate. *Phys. Solid State* **2003**, *45*, 41–45. [CrossRef]
28. Martynov, S.; Petrakovskii, G.; Boehm, M.; Roessli, B.; Kulda, J. Spin-Wave Spectrum of Copper Metaborate in the Incommensurate Phase. *J. Magn. Magn. Mater.* **2006**, *299*, 75–81. [CrossRef]
29. Kopteva, N.E.; Kudlacik, D.; Yakovlev, D.R.; Eremin, M.V.; Nurmukhametov, A.R.; Bayer, M.; Pisarev, R.V. Zeeman and Davydov Splitting of Frenkel Excitons in the Antiferromagnet CuB2O4. *Phys. Rev. B* **2022**, *105*, 024421. [CrossRef]

30. Abragam, A.; Bleaney, B. *Electron Paramagnetic Resonance of Transition Ions*; Oxford Classic Texts in the Physical Sciences; Oxford University Press: Oxford, UK, 2012; ISBN 978-0-19-965152-8.
31. Eremin, M.V. On the Theory of Magnetoelectric Coupling in $LiCu_2O_2$. *J. Exp. Theor. Phys.* **2019**, *129*, 990–997. [CrossRef]
32. Eremin, M.V. Coupling of Spins with an Electric Field in FeV_2O_4. *Phys. Rev. B* **2019**, *100*, 140404. [CrossRef]
33. Shuai, D.; Jun-Ming, L.; Sang-Wook, C.; Zhifeng, R. Multiferroic materials and magnetoelectric physics: Symmetry, entanglement, excitation, and topology. *Adv. Phys.* **2015**, *64*, 519–626. [CrossRef]
34. Takahashi, Y.; Shimano, R.; Kaneko, Y.; Murakawa, H.; Tokura, Y. Magnetoelectric resonance with electromagnons in a perovskite helimagnet. *Nat. Phys.* **2012**, *8*, 121–125. [CrossRef]
35. Kida, N.; Ikebe, Y.; Takahashi, Y.; He, J.P.; Kaneko, Y.; Yamasaki, Y.; Shimano, R.; Arima, T.; Nagaosa, N.; Tokura, Y. Electrically driven spin excitation in a ferroelectric magnet $DyMnO_3$. *Phys. Rev. B* **2008**, *78*, 104414. [CrossRef]